ENVIRONMENTAL STUDIES

Human perturbations to mercury in global rivers

Dong Peng[1,2], Zeli Tan[3], Tengfei Yuan[4], Peipei Wu[5], Zhengcheng Song[2], Peng Zhang[2], Shaojian Huang[2], Yanxu Zhang[4]*, Ting Lei[6], Beth A. Middleton[7], Jeroen E. Sonke[8], Guangchun Lei[6], Jianhua Gao[1]

Mercury compounds are potent neurotoxins that pose threats to human health, primarily through fish consumption. Rivers, critical for drinking water and food supply, have seen rapid increases in mercury concentrations and export to coastal margins since the Industrial Revolution (~1850). However, patterns of these changes remain understudied, limiting assessments of environmental policies. Here, we develop a global model to simulate preindustrial riverine total mercury and assess human perturbations by comparing it to present-day conditions. We find that global rivers transported ~390 megagrams annually of mercury to the oceans in the preindustrial era, with spatial variability. Human activities have elevated riverine mercury budgets by two to three times in the present day. Establishing a baseline riverine mercury level, our findings reveal rapid responses of riverine mercury to human perturbations and could be used to inform targets for global riverine mercury restoration. Total riverine mercury concentrations could also be used as indicators to comprehensively understand the effectiveness of mercury pollution governance.

INTRODUCTION

Highly toxic mercury (Hg) compounds (*1*), especially methylmercury (MeHg), are regulated by the Minamata Convention on Mercury (hereafter referred to as the Minamata Convention) that took effect in 2017 (*2*). Hg compounds originate from both natural sources, such as volcanic degassing, and human-induced emissions and releases, including coal combustion, metal mining, artisanal and small-scale gold mining (ASGM), and industrial manufacturing (*3*). These sources release Hg into the atmosphere, land, and water, forming an intricate biogeochemical cycle (*4*), with rivers playing a pivotal role as major conduits for the transfer of Hg from terrestrial to marine environments (*5*). Rivers also profoundly influence human exposure to Hg because aquatic products, the consumption of which is the major Hg exposure pathway (*6*), are primarily sourced from wild-catching and aquaculture activities in inland waters and near-shore environments (*7*–*9*). In addition, rivers and coastal wetlands serve as vital habitats for diverse wildlife (*10*), leading to efforts to protect these areas from Hg pollution (*11*), as highlighted by the Ramsar Convention on Wetlands and the Convention on Biological Diversity (*8*, *9*).

Riverine Hg undergoes complex biogeochemical processes, with most Hg bound to suspended particulate matter (SPM; or, i.e., microscopic particles in water), such as 90% particulate phase of Hg in the Yukon River and >70% in the Yangtze River (*12*, *13*). While human-induced Hg releases are important sources of Hg in rivers in the present day (*14*), soil erosion was the major source during the preindustrial era, which was influenced by the soil Hg contents, texture and erodibility, land cover/scape, precipitation, and runoff (*12*, *15*). Atmospheric deposition serves as a source of Hg to rivers; however, short-term Hg fluxes from the atmosphere to rivers via air-water exchange remain minimal (*16*). Over the long term, atmospheric deposition primarily contributes to riverine Hg through its effect on elevating soil Hg concentrations, as soil, with its larger exchange area, plays a more dominant role than direct water exchange within the watershed. Riverine particulate Hg is subjected to settling and resuspension in the riverbeds (*12*), which is affected by the different attributes of rivers such as their slopes, water velocity, runoffs, and bedrock characteristics (*17*, *18*). Most riverine Hg bound to SPM is effectively exported downstream into the coastal environment without dam blocking such as in the preindustrial era (*13*, *19*, *20*), when most riverine Hg was buried in coastal sediment (*7*, *21*).

Human activities have perturbed the riverine Hg budget (the gross riverine Hg fluxes to oceans), evidenced by the dated sediment records in river channels and estuaries (*22*–*24*). It is estimated that up to 1540 Gg of Hg had been released into the environment due to human activities from 2000 BCE to 2010 CE, of which 1130 Gg were released (336 Gg to air and 790 Gg to land/water) during the 1850–2010 period (*25*), so that most Hg was released to land/water. It was estimated that about 20% of the Hg released could enter the river systems (*26*), i.e., ~150 Gg has been released into the water. Some of the rivers in different regions have become among the most polluted ecosystems due to the marked increases in wastewater input and soil erosion (*8*, *12*, *27*–*29*). Meanwhile, the building of dams and reservoirs has played an important role in the riverine processes, because dams act as barriers for SPM and result in enhanced Hg storage in global rivers (*12*, *15*). Taking the Yangtze River as an example, only about 30% of the riverine Hg flux can pass the Three Gorges Dam to downstream areas (*12*, *15*). It is estimated that more than 100 billion metric tons of sediment has been retained in reservoirs since 1850 (*18*). Earlier studies, such as Selin *et al.* (*30*), estimated the preindustrial riverine export of all types of Hg to oceans at 40 Mg/year using a box model; however, this assumption lacked observational constraints and spatial resolution. Riverine processes were usually ignored in global Hg models, and the baseline of the riverine Hg budget is thus lacking (*6*, *19*, *21*, *31*).

Here, we develop a process-based river Hg model (MOSART-Hg) based on the MOdel for Scale Adaptive River Transport (MOSART)

[1]School of Geography and Ocean Science, Ministry of Education Key Laboratory for Coast and Island Development, Nanjing University, Nanjing, China. [2]School of Atmospheric Sciences, Nanjing University, Nanjing, China. [3]Pacific Northwest National Laboratory, Richland, WA, USA. [4]Department of Earth and Environmental Sciences, Tulane University, New Orleans, LA, USA. [5]Scripps Institution of Oceanography, University of California San Diego, La Jolla, CA, USA. [6]School of Ecology and Nature Conservation, Beijing Forestry University, Beijing, China. [7]U.S. Geological Survey, Wetland and Aquatic Research Center, Lafayette, LA, USA. [8]Géosciences Environnement Toulouse, CNRS/IRD/Université de Toulouse, Toulouse, France.
*Corresponding author. Email: yzhang127@tulane.edu

included in the Community Earth System Model version 2.1.3 (CESM2) to simulate the total riverine Hg budget in the preindustrial era (*32*) (refer to the Materials and Methods). The model includes the soil Hg erosion processes and the riverine transport of Hg to oceans. The empirical relationships between precipitation events, runoff, soil erosion, and soil Hg dynamics are considered in this model, based on previous studies (*13*, *15*, *19*, *33*). The model results are evaluated against published coastal and estuarine sediment records of Hg collected worldwide. We also assess the human perturbation of the global riverine Hg budget by comparing the simulated preindustrial budget with the present-day Hg budget derived from observations and models. The objectives of this study are to (i) introduce the processes-driven model for riverine Hg simulation, (ii) establish the riverine Hg dynamics in the preindustrial era, and (iii) provide an assessment of riverine Hg pollution from the preindustrial to the present day.

RESULTS

Riverine Hg budget in 1850

The modeled global erosional flux of soil Hg for the 1845–1859 simulation period is 397 ± 8.1 Mg/year, representing the mean ± SD and serving as the major source of Hg for preindustrial rivers (Fig. 1A). This flux was calculated by the Hg-embedded soil erosion processes of land components of the model, which consider the erosion driven by rainfall and runoff and the deposition of eroded material in the hillslope (refer to the Materials and Methods). The erosional sources of riverine Hg are affected by the spatial distribution of soil Hg concentrations on land (fig. S1). We set the global soil Hg concentration dataset based on Selin *et al.* (*30*) for the preindustrial era. We also assume that the soil Hg concentration had not changed during the 1845–1859 simulation period, which is reasonable given the large mass of Hg stored in the land (up to 1×10^6 Mg) (*30*).

Erosional Hg fluxes were the major sources of riverine Hg in the preindustrial period but may no longer dominate in the present day due to high-level releases from anthropogenic Hg sources. The changes in erosional Hg fluxes from preindustrial to present day are relatively small (fig. S2), as they are constrained by limited variations in soil Hg and sediment yield. However, the magnitude of anthropogenic Hg releases surpasses natural sources. For instance, previous estimates suggest that ~7300 Mg/year of Hg has been released to land and water (*25*).

In general, higher Hg erosion is simulated in the 30°N to 30°S region due to intense subtropical precipitation and highly erodible highlands (Fig. 1B). Notably, interannual and seasonal variability for the erosion of Hg and riverine Hg budget are simulated at both global and regional scales (figs. S3 to S6). The higher erosional fluxes of soil Hg are mostly simulated in highlands with relatively high precipitation and/or runoff (fig. S7). For example, the Himalayan mountains (average altitude: 6096 m; highest altitude: 8849 m) have the highest contribution of soil Hg fluxes to rivers. The larger difference in altitude between the Himalayan mountains and the nearby regions is the precondition to the formation of giant rivers, such as the Yangtze, Yellow, and Brahmaputra Rivers. These energetic rivers have strong erosional power and deliver sediment downstream, contributing to high Hg erosion fluxes in Asia. These rivers are also the major riverine Hg exporters to oceans in the present day (*5*).

Likewise, the Andes Mountains (average altitude: 3962 m; highest altitude: 6962 m), East African Plateau (~1000 m; 5895 m), Brazilian Plateau (~1000 m; 2993 m), and Mexico Plateau (1825 m; 5636 m) cause comparatively elevated Hg erosion fluxes. Specifically, in mountainous regions near the coasts, such as the Andes Mountains and the Barisan Mountains (Sumatra Island) (~2400 m; 3805 m), the combination of extensive basin areas, high elevations, and steep slopes results in high sediment loading. This is also true for relatively small mountain rivers, such as the Salinas River (California, USA) (*34*). Many of these rivers flow directly into active margins (coast and estuary) (*35*) and can swiftly deliver erosional Hg and SPM to the coast within hours or days after precipitation (*36*). Flood deliveries of erosional Hg are short-lived events, often challenging to sample, and therefore difficult to observe. For instance, the Hg concentration and flux in flooding waves in the Vistula River changed very fast by observation, while the flooding wave only lasted 2 to 3 days (*36*). Consequently, their global contribution to soil erosion Hg flux has often been overlooked.

The modeled riverine Hg fluxes are influenced by the SPM loads of the rivers and the SPM-Hg concentrations, which are controlled by the soil Hg contents (Fig. 1C). The model suggests that the Nile, Yangtze, Amazon, Ganges, and Mekong rivers have higher riverine Hg fluxes than other rivers. Both the Nile and Yangtze rivers had high sediment loading before the giant dams were constructed (e.g., the Aswan High Dam in the Nile River and the Three Gorges Dam in the Yangtze River). Taking the Nile River as an example, the large riverine Hg flux is primarily attributed to its extensive watershed compared to other rivers and the resuspension of settled sediments. The sediments in the Nile River are mostly originate from Ethiopia (>95%), 60% of sediment fluxes of the mainstream are delivered by the Blue Nile, and in the Blue Nile, its flow velocity is highly correlated with SPM and bedload, contributing to the suspended loads (*37*, *38*). More than 22 Mg/year of riverine Hg settles within the Nile River bed, accounting for 48% of the Nile River watershed gross erosional Hg budget (referred to as the deposition Hg ratio, to represent the annual Hg storage in the river channel divided by the annual gross erosion flux of the corresponding watershed; table S1). We also calculate that the settled Hg in the riverbeds accounted for 49% of the total input riverine Hg (referred to as the bedload Hg ratio, representing the annual Hg storage in the river channel divided by the annual gross riverine Hg export flux of the corresponding river; table S1). Note the differences in the deposition Hg ratio and bedload ratio caused by the settling or resuspension of Hg along the hillslopes.

Several other rivers exhibit high riverbed Hg settling in our model. For instance, the Amur, Mackenzie, Mekong, Yellow, and Ob Rivers all have deposition Hg ratios exceeding 30% and bedload Hg ratios surpassing 20% (table S1). In contrast, the Amazon River, Amu Darya River, Colorado River, Helmand River, Mississippi River, Parana River, Rio Grande, and Congo River have less Hg settled in the riverbed, characterized by relatively lower deposition Hg ratios (<10%) and bedload Hg ratios (<10%) in the model.

The modeled preindustrial riverine Hg export to oceans is influenced by the watershed Hg erosion and riverine transport efficacy, which are influenced by the river flow and flow speed. The model simulates a global river Hg export flux of 390 Mg/year (range: 321 to 483) to the coastal oceans (including inland lakes) in 1845–1859 (Fig. 1D). Compared to the global soil Hg erosion flux of 397 Mg/year, this implies an overall high efficiency of riverine transport and export (98%, bedload Hg not considered). There is only about 7 Mg/year Hg, calculated as the difference between the modeled global erosion and export fluxes, settled in the bedload of sheet flow or the

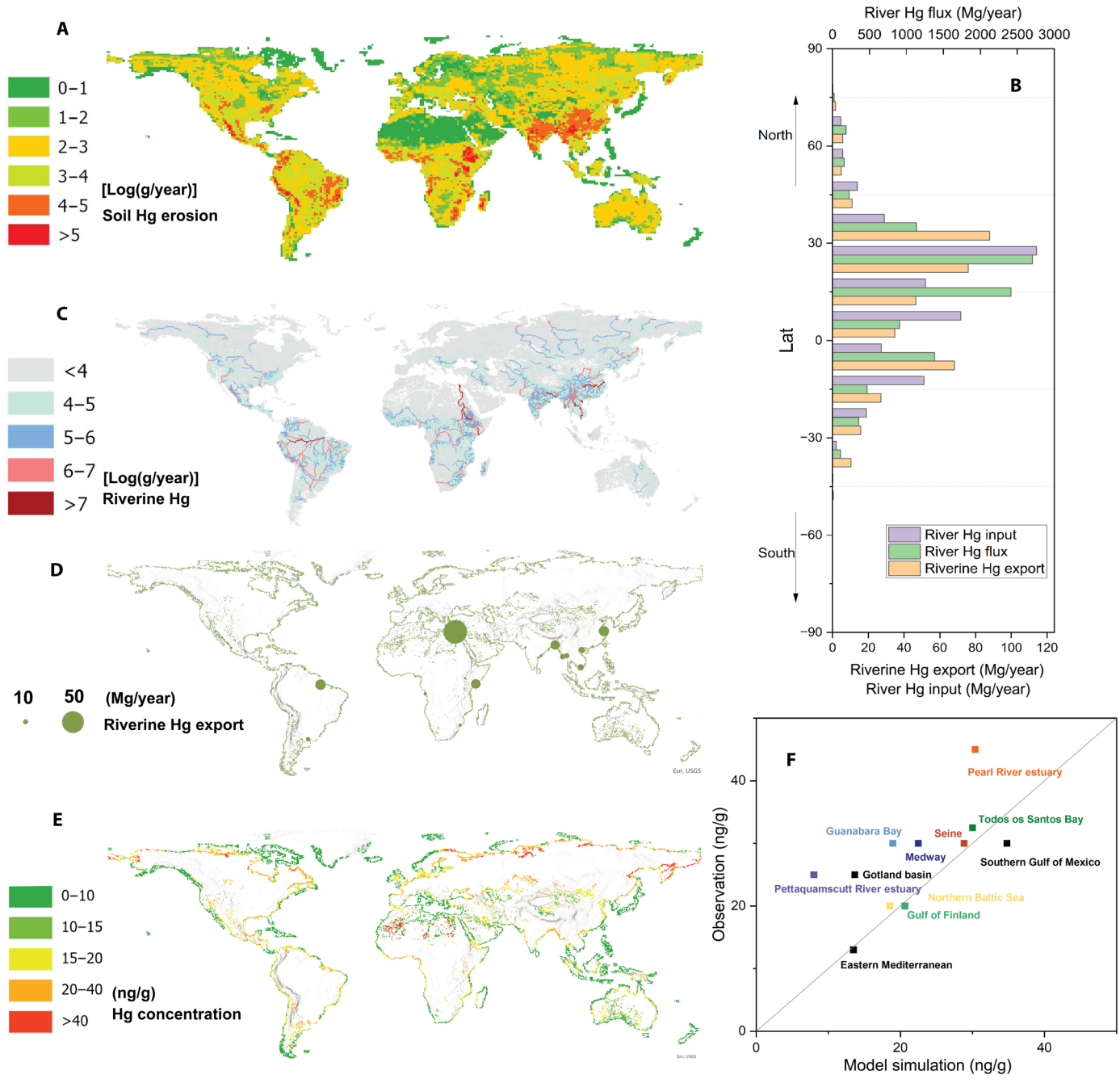

Fig. 1. Global riverine Hg budget for the preindustrial era. (**A**) Soil erosion flux from land to runoff. (**B**) Mean latitude distribution of riverine Hg flux. Lat, latitude. (**C**) Hg fluxes in rivers. (**D**) Export flux of Hg to the coastal ocean. (**E**) Hg concentration in SPM at river mouths. (**F**) Comparison of modeled Hg concentrations in SPM against preindustrial Hg concentrations in dated sediment records near river mouths.

river channels. The modeled riverine export of Hg is primarily affected by the multiyear erosional Hg budget of the watershed. Even when a river exhibits lower transport efficiency, settled SPM and Hg can still be resuspended as a source once the storage capacity is reached (i.e., sediments have settled and equilibrated in the riverbed; fig. S4) (*39*). For example, the Nile River contributes the most (53 Mg/year) to the riverine Hg export globally, although its watershed's mean Hg erosion budget is only about 46 Mg/year, demonstrating that the bedload acts as an important Hg source of 7 Mg/year.

Throughout long-term preindustrial simulations (15 to 20 years), the riverine Hg export budgets tend to align closely with the mean erosion budgets of the corresponding watersheds. Consequently, our model suggests that rivers located in highland areas that have larger multiyear erosional Hg budgets exhibit relatively higher riverine Hg exports, e.g., those rivers in proximity to the Tibetan Plateau and the Deccan Plateau in Asia, such as Yangtze River (23 Mg/year), Ganges-Brahmaputra Delta (20 Mg/year), Mekong River (13 Mg/year), and others (table S1). Similarly, rivers near the western Guinea Plateau

and East African Plateau in Africa also have higher riverine Hg export, such as the Congo (6 Mg/year). In North America, rivers near the Mexico Plateau exhibit elevated Hg levels, while in South America, rivers near the Andes Mountains and the Brazilian Plateau also play a notable role, such as the Amazon (23 Mg/year).

We find that these high-export rivers are not necessarily the largest rivers, and small mountain rivers also contribute to the global Hg export to oceans, such as the west coast of South Central America. An illustrative pattern emerges in rivers along the west coast of Mexico, as exemplified by Rio Yaqui (2.46 Mg/year) and Rio Santiago (3.30 Mg/year), both demonstrating a comparatively higher riverine Hg export to the coast than larger rivers such as the Colorado River (2.18 Mg/year). Similarly, rivers along the west coast of South America, such as Rio Chira in Peru (2.43 Mg/year), exhibit a parallel trend with elevated riverine Hg export to oceans.

The exported preindustrial Hg concentrations in the SPM (ng/g) at river mouths and inland lakes are calculated as the ratio of the export fluxes of Hg and SPM (Fig. 1E), which are largely determined by the soil Hg contents in the corresponding watersheds. The model suggests that the coast in the high latitudes in the Northern Hemisphere such as the Russian Arctic has a much higher exported Hg concentration than the coast of the Southern Hemisphere. The estuaries of the Ob and Yenisei rivers and the rivers in the Russian Far East export high riverine Hg concentration to the near coast (>40 ng/g) than other regions due to the relatively lower SPM load and high peat soil Hg concentrations (refer to fig. S1). The lakes that are in the surrounding of the Sahara Desert also have high simulated riverine Hg concentrations (>40 ng/g). The model simulates lower Hg concentrations at the coast of many islands, the west coast of North America, and the coast of the East China Sea because of the lower soil Hg contents in the corresponding watersheds.

We compare the simulated preindustrial exported Hg concentrations against published sediment core records dated back to ~1850 (Fig. 1F). The sediment cores were collected from diverse locations, spanning the Eastern Mediterranean, Gulf of Finland, Seine River, and Southern Gulf of America, representing a global array of estuaries. We assumed that the dominant form of Hg discharged by these rivers is in SPM and settled in estuaries. Rivers are also assumed as the only source of Hg to estuaries in the preindustrial era within the model. The Hg concentrations in the sediment records of the preindustrial era mostly ranged from ~10 to 45 ng/g, dating back to ~1850 or earlier, as determined by the 210-lead isotope method, and were regarded as background levels (table S2). We find that the simulated exported Hg concentrations agree well with the sediment records in both magnitude and spatial patterns. The Hg concentrations in the upper layers of sediment cores after 1850 display much higher levels than in the preindustrial era, such as in Coronel Bay (Chile) and the Pettaquamscutt River estuary (table S2), underscoring the impact of anthropogenic Hg release since the Industrial Revolution. Some cores, such as those from the Pettaquamscutt River estuary, reveal human influences dating back to the early 1800s and exceed our model estimates, showing a rapid increase in Hg concentration after 1830, with an initial peak around 1850 resulting from early industrial activities in this region (*40*). We thus use the ~1800 baseline levels from these cores for our model evaluation. The model shows a slightly larger discrepancy for some of the smaller rivers, likely caused by the model's representation of the related topography, hydrology, meteorology, and soil characteristics, but the discrepancy is generally within the random errors of the sediment sampling, dating, and Hg measuring methods (*41*). Furthermore, the MOSART simulates 15.1 Gt/year of sediment export in the preindustrial era, which is also close to previous observational and model studies (fig. S8) (*20*), indicating that our estimate of global riverine Hg export is reliable.

Human perturbation of global river Hg export

We find that the global riverine Hg budget potentially increased by a factor of 2 to 3 due to human perturbation since the preindustrial era (Fig. 2). We use the simulated riverine Hg budget in the preindustrial era as the baseline to compare with present-day riverine Hg discharge inventories from observations. Amos *et al.* (*19*) estimated a high global riverine total Hg discharge of 5500 Mg/year, largely driven by uncertain and potentially overestimated contributions from Asian rivers (*21*). In contrast, Liu *et al.* (*21*) updated the global riverine total Hg budget to 1000 Mg/year (range: 893 to 1224 Mg/year) based on more recent data and a more comprehensive statistical fitting approach (referred to as the "Liu budget"). Compared to the Liu budget, our MOSART Hg budget indicates an increase of 595 Mg/year since the preindustrial era, representing a two- to threefold growth in river Hg export (Fig. 2).

We also compare the simulated preindustrial Hg levels to the modeled results in the present day (*26*). The present-day simulation builds on the preindustrial model, incorporating additional processes such as anthropogenic Hg release, the effects of reservoirs and dams, and using present-day meteorological, hydrological, land use/cover, and soil Hg datasets. The present-day model simulates a similar riverine Hg budget to the global ocean of ~1000 Mg/year (range: 777 to 1146 Mg/year). Unlike the observation-based data prediction and training methods used in Liu budget, the present-day simulation incorporates the spatial distribution of anthropogenic Hg sources as model inputs, tracking their pathways from land to oceans. This approach helps fill gaps in regions with limited observations and improves estimations, particularly for smaller rivers. Moreover, unlike Liu budget, our method provides a source-sink framework for Hg cycling in terrestrial rivers. While the agreement between the present-day model and observations demonstrates the model's predictive accuracy, the differences between the present-day and preindustrial simulations reveal the scale and distribution of human perturbation in riverine Hg levels (Fig. 2).

The substantial augmentation in the global riverine Hg budget from the preindustrial era to the present quantifies alterations in Hg release resulting from industrial and other anthropogenic activities. First, it has been estimated that there was an ~15% increase in average topsoil (0 to 15 cm) Hg concentrations across the global land from the preindustrial to the present day due to enhanced atmospheric Hg deposition (*30*), contributing to higher Hg inputs into global rivers via erosion (figs. S2 and S8). Second, the direct wastewater discharged into rivers from both domestic and industrial sources led to an increase in riverine Hg (*14*, *42*). For instance, an estimated 162 Gg of Hg has been discharged into water bodies between 1850 and 2010 due to commercial Hg usage (*14*), equating to a mean annual release of ~950 Mg over the 170-year period. This stands in stark contrast to the preindustrial era, during which we estimate riverine Hg exports were ~400 Mg annually.

The development of dams altered the sediment settling and resuspension patterns, decreasing riverine transport efficiency (*12*, *15*). The estimations of sediment flux export to oceans in 1950 and 2010 are 15.7 and 8.5 Gg annually, respectively, implying that a minimum of 40% of sediments has been retained by dams during this period

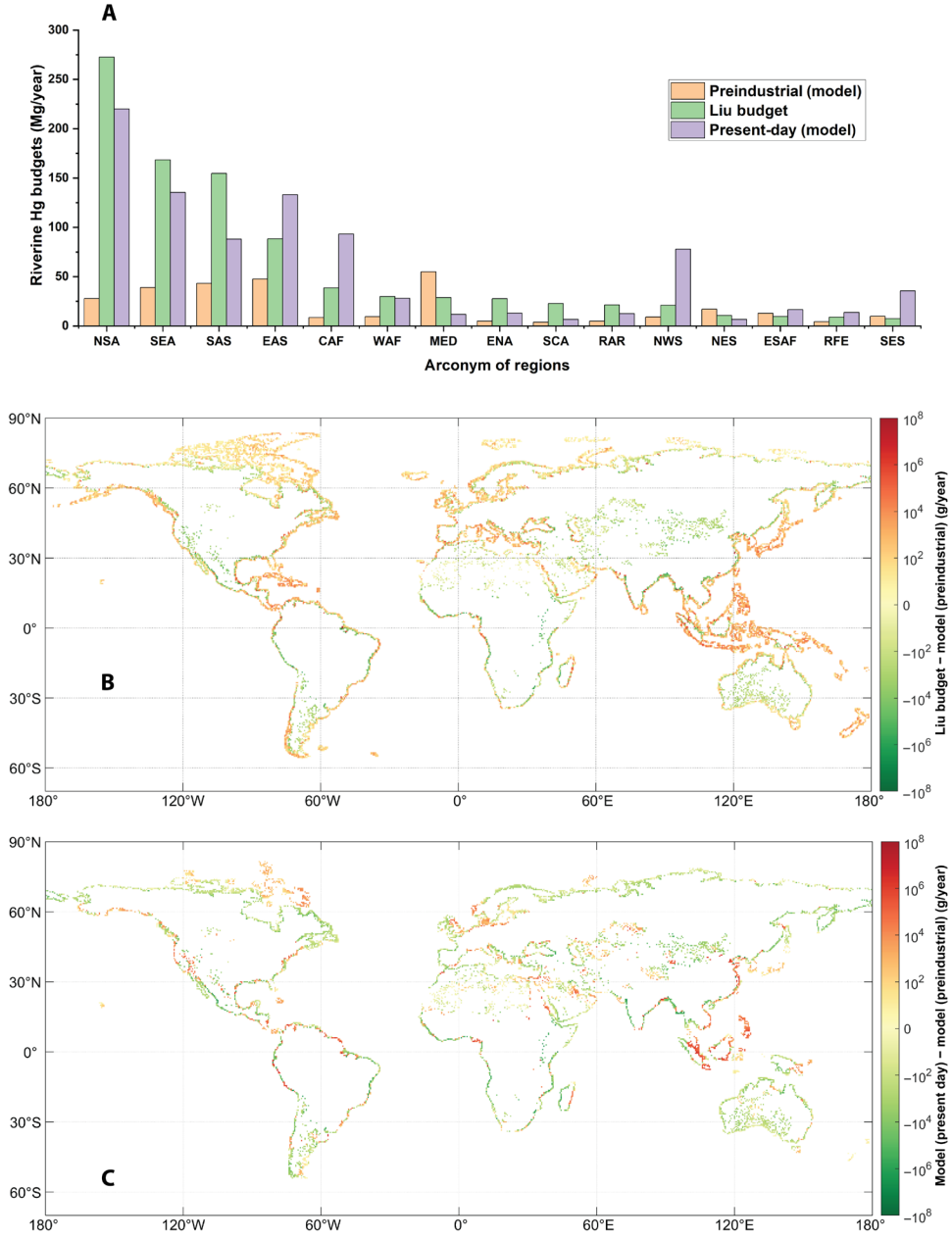

Fig. 2. Changes in the global riverine Hg budget from the preindustrial era to the present day. (**A**) Riverine Hg budgets of simulations in some Intergovernmental Panel on Climate Change WGI reference regions. The regions include North South America (NSA), Southeast Asia (SEA), South Asia (SAS), East Asia (EAS), Central Africa (CAF), Western Africa (WAF), Mediterranean (MED), East North America (ENA), South Central America (SCA), Russian Arctic (RAR), Northwest South America (NWS), Northeast South America (NES), East Southern Africa (ESAF), Russian Far East (RFE), and Southeast South America (SES). (**B**) Differences between model simulation in the preindustrial era and Liu budget (*21*). (**C**) Differences between model simulation in the preindustrial era and the present day (*26*).

(*18*, *20*). In addition, the previously settled sediments could have higher Hg concentration than the newly settled sediments, the resuspension of which could cause higher riverine Hg export to oceans (*12*, *15*). For instance, an analysis of dated sediment cores from Todos os Santos Bay in Northeast Brazil revealed notable elevated Hg concentrations in deeper layers corresponding to the approximate time frame of the 1980s (*24*).

These factors exhibit considerable spatial heterogeneity, and their relative importance varies across regions, resulting in changes in regional riverine Hg budgets within Intergovernmental Panel on Climate Change Sixth Assessment Report Working Group I (IPCC AR6 WGI) reference regions (Fig. 2A) (*43*). On the basis of the Liu budget, North and South America became the largest contributor (41%, 245 Mg/year) to the global Hg river export growth, compared to the preindustrial era, followed by Southeast Asia (22%, 130 Mg/year) and South Asia (19%, 111 Mg/year) (Fig. 2B). The modeled differences between the present day and the preindustrial era have similar export patterns with the largest contributions also from

North and South America (31%, 192 Mg/year) and Southeast Asia (16%, 97 Mg/year), followed by East Asia (14%, 86 Mg/year) to the global riverine Hg export growth (Fig. 2C) (*26*). Regions experiencing rapid growth in Hg releases, particularly those with poorly managed ASGM activities, highlight the profound impact of the ASGM sector. Notably, ASGM has become the largest contributor to Hg releases across all sectors [Arctic Monitoring and Assessment Programme (AMAP)/UN Environment Programme (UNEP), 2019]. The Amazon watershed in South America exemplifies this trend. The marked increase in riverine Hg fluxes in North and South America is linked to higher erosional Hg inputs into the Amazon River. Because of land-use changes, erosional Hg fluxes in the Amazon have doubled from the preindustrial era to the present day. In a scenario without human-induced Hg releases, the Amazon's riverine Hg budget would have increased from 25 Mg/year (preindustrial) to 46 Mg/year (present day) solely due to intensified erosion. This rise is driven, in part, by deforestation, as ~20% (788,353 km^2) of the Amazon has been cleared over the past 60 years (*26*), leading to increased soil erosion. However, the impact of human-induced Hg releases in this region is even more pronounced. Because of rapidly increasing anthropogenic releases, the Amazon River's Hg budget now exceeds 200 Mg/year, with three-quarters of this originating from human activities and primarily ASGM.

Some regions experienced an even lower riverine Hg budget in the present day than during the preindustrial era. For example, the present-day Hg budget for the Mediterranean region is 26 Mg/year lower than that during the preindustrial era based on the Liu budget (43 Mg/year lower based on our present-day simulation) (table S3). This pattern may be attributed to the impact of dam-induced trapping effects within the Nile River watershed, exemplified by sediment retention in structures such as the Aswan High Dam and other upstream reservoir systems. Rivers with lower anthropogenic Hg releases and increased dam construction are likely to face similar decreases in riverine Hg budgets in the present day.

Our analysis reveals the role of key Hg sources such as ASGM in determining the riverine Hg budget. The substantial contribution from South Central America is primarily driven by ASGM (*3*, *25*). In countries with a higher fraction of Hg loss per unit of gold production, such as Honduras (*44*), high levels of Hg releases from ASGM have driven a ~6-fold increase in riverine Hg flux between 1850 and 2010 (from 4 to 22 Mg/year in the Liu budget). The rate of increase is also high in Southeast Asia (3 to 4; 39 versus 169 Mg/year of Liu budget, 135 Mg/year in the present day). ASGM activities emerge as an important factor in this region, contributing to an annual discharge of more than 300 Mg of Hg into water ecosystems (*3*, *45*). Besides, the increase in riverine Hg fluxes in rivers is associated with the increase in Hg concentration in the soil and water and the high sediment loading exported to oceans (*46*, *47*). Similarly, the present-day simulation shows higher growth in riverine Hg export in Central Africa (+30 Mg/year in the Liu budget versus +85 Mg/year in the present-day simulation), northwestern South America (+12 Mg/year versus +69 Mg/year), and southeastern Africa (−2 Mg/year versus +26 Mg/year) than in the Liu budget (Fig. 2, B and C, and table S3). These regions also experience high Hg releases and emissions from ASGM but have weaker industrialization (Fig. 2, B and C) (*3*). The discrepancy between the model and the Liu budget might be caused by the lack of observations in these regions. The potential difference in the Liu budget for South Asia (+111 Mg/year versus +45 Mg/year by the simulation) also highlights how observational records of riverine Hg in these regions could refine model predictions.

Industrial Hg releases are the primary driver of riverine Hg increases in regions such as East Asia. Observations indicate that rivers in China contribute more than 70% of the riverine Hg budget in East Asia (*5*). Hence, the elevated riverine Hg fluxes in East Asia (+41 Mg/year in Liu budget versus +86 Mg/year in this study) are largely attributed to industrial Hg releases. The Yangtze River exemplifies this trend. Its riverine Hg flux has increased from 22.5 Mg/year (preindustrial) to 48 Mg/year (Liu budget), highlighting the contribution of industrial releases within its watershed. In contrast, ASGM-related Hg releases are negligible due to strict legal regulations in China. In addition, the Three Gorges Dam plays a crucial role in regulating Hg transport, blocking more than 50% of riverine Hg from reaching downstream (*15*).

The human perturbation to the riverine Hg budgets aligns with increasing Hg trends observed in the atmosphere and ocean since the Industrial Revolution (around 1850), characterized by enrichment (*25*, *48*). The present-day atmospheric Hg levels are generally considered to have increased by a factor of 3 since preindustrial times, evidenced by lake sediment records that have atmospheric deposition as the major input (*49*). A similar level of enrichment is found for the surface ocean due to its fast exchange with the atmosphere (*50*). While the enrichment ratios in the atmosphere and surface ocean largely reflect the atmospheric emissions from sources such as coal burning and mining, the enrichment in the rivers is more driven by the Hg input via wastewater release from chemical manufacturing, Hg-contained produce usage, and gold mining, which have different historical trajectories from 1850 to 2010 (*25*).

Compared with the relatively homogeneous atmosphere and ocean Hg budgets, land-river systems have much higher spatial heterogeneity and thus show more regional variabilities, reflecting the local input from soil erosion and wastewater discharge. More riverine and estuarine sediment records could help to reveal the scale and pattern of human perturbation to the riverine Hg budgets.

Uncertainty analysis

Our model results bear uncertainties because of limitations in the resolution of the global datasets and models. The relatively coarse resolution (0.9° latitude × 1.25° longitude) cannot fully resolve the soil erosion processes and its influencing factors, such as small-scale topography and land cover changes (refer to the Materials and Methods). As computing power continues to improve, there is substantial potential for advancing global soil erosion simulations, thereby enhancing the accuracy of erosional Hg flux simulations. Our Hg model is built on the basis of the simulation of erosion processes and the riverine water/sediment budgets of MOSART, the uncertainties of which are mostly inherited for the budget of Hg (*51*–*53*). The sensitivity experiments provide insights into the constrained model bias stemming from resolution discrepancies for sediment flux (fig. S8), thereby constraining the uncertainties for riverine Hg flux, as well as the bias from the soil Hg concentration dataset (fig. S9) and Hg deposition/escape processes (fig. S10) (refer to the Materials and Methods).

The erosion processes estimated in this study are based on an improved version of the Morgan model (refer to the Materials and Methods) tailored for Earth system models, exhibiting a superior capacity to elucidate spatial variability in sediment yield when compared to other models such as the Revised Universal Soil Loss Equation (RUSLE) model (*33*, *54*). The improved Morgan model has been

validated and can well explain erosion processes with soil carbon simulation (*51*). This model also has a 59% lower discrepancy compared with observations than the other hydrology models, such as the RUSLE model, in the present-day simulation (*54*). Recognizing the potential limitations of the improved Morgan model, we use the sediment fluxes derived from the BQART model (global sediment load model) to constrain the original erosion fluxes of sediment in our simulation (refer to the Materials and Methods) (*20*), which aligns well with observed Hg concentrations in estuaries (Fig. 1F and fig. S7).

Potential limitations in the simulation may also arise from the soil Hg concentration dataset, as it assumes uniform soil Hg concentrations within the 0- to 15-cm-depth range. However, given that soil erosion predominantly occurs in the surface soil layer, the uncertainties associated with the vertical distribution of soil Hg concentrations can be deemed acceptable. The model does not consider the soil Hg concentration changes by leaching, erosion, and atmospheric deposition, which might be an important factor for longer model simulation periods (refer to the Materials and Methods and fig. S10). Chemical transformations among different Hg species and air-river Hg exchange within river channels are omitted because of their minimal influence on the overall Hg budgets (see the Materials and Methods and fig. S10).

The uncertainties of the processes that govern the riverine sediment routing and their evaluation against observations are presented in previous studies (*52*). The validated sedimentation and resuspension processes within the Earth system model are applicable to Hg dynamics, given that riverine Hg is predominantly associated with SPM (refer to the Materials and Methods), but certain sedimentary processes, such as grain size alteration, are not considered in the context of Hg dynamics. Besides, the complicated reservoir trapping processes are not included in our simulation due to the scenario of preindustrial era. In terms of the runoff driving factors, the absence of comprehensive datasets relating to the preindustrial era may introduce additional uncertainties. For instance, the meteorology forcing, commencing from 1900, may not accurately reflect climate conditions around 1850. However, its direct impact on riverine Hg budgets is limited, given the negligible atmospheric deposition of Hg to water surfaces during the preindustrial period and the atmospheric deposition to watersheds has mostly been identified as the changes of soil Hg concentration in the model simulations (refer to the Materials and Methods and figs. S9 and S10). The model also incorporates present-day river channel distributions, resulting in less precise simulations for rivers such as the Yellow River, which have experienced channel changes over time.

DISCUSSION

Implications

Rivers assume a pivotal role in the biogeochemical cycle of Hg and constitute a substantial component of the overall Hg budget. As a linkage between the land and ocean, the export of riverine Hg to oceans is estimated as ~400 Mg/year during the preindustrial era, which is comparable with the atmospheric Hg deposition to oceans (500 Mg/year) at that time (*25*). Rivers play an even more important role in the present day than during the preindustrial era, representing a factor of 2 increase and contributing ~1000 Mg/year to oceans (*21*). Its impact on the cycling of Hg in oceans and other environmental compartments cannot be neglected. In addition, riverine Hg serves as a crucial source for remote coastal wetlands and the Arctic Ocean, thereby contributing to substantial Hg exposure in such less-polluted regions (*19*, *21*, *55*). Moreover, our study reveals that the levels of riverine Hg are sensitive to human activities, which reflect the intensity of human-induced perturbations, including alterations in land cover, climate change, and the outcomes of environmental policies.

Over the period from 1850 to the present, human activities have exerted influence on riverine Hg fluxes, consequently elevating Hg levels and posing ecological risks to both human populations and wildlife. The consumption of freshwater fishes and associated products emerges as a notable pathway for Hg exposure, carrying inherent risks to human health (*6*). Elevated concentrations of Hg in rivers can be discharged into both inland and coastal wetlands, posing a threat to wildlife (*11*). These wetlands, acknowledged for their high biodiversity and ecological significance as wildlife habitats (*10*), can be particularly vulnerable to the detrimental effects of Hg contamination, potentially leading to the degradation of their fragile ecosystems.

The coastal wetlands in East and Southeast Asia are experiencing an increase in riverine Hg (Fig. 2, B and C), which could potentially harm the migratory habitats in the East Asian–Australasian Flyway (*56*), one of the most crucial flyways for wetland birds globally. Similarly, the increased riverine Hg in the coastal wetlands of the west coast of the Pacific and the Gulf of America threatens habitats in the Pacific Flyway, Mississippi Flyway, and Atlantic Flyway (*57*). Consequently, assessing human perturbation on changes in riverine Hg is crucial for pollution restoration, with potential benefits for human health, biodiversity conservation, and wetland protection.

The establishment of a baseline for riverine Hg budgets during the preindustrial era serves as a fundamental reference point, providing a framework for contemporary objectives in international agreements such as the Ramsar Convention on Wetlands (*58*), the Convention on Biological Diversity (*59*), and the Minamata Convention (*60*). While the Minamata Convention's Hg phaseout initiatives have effectively reduced Hg emissions in various regions, some areas are experiencing increased Hg release from ASGM in South Asia, Southeast Asia, and South America. In a global context, the established baseline for the riverine Hg budget may serve as a potential objective for nations worldwide in efforts toward the reduction of Hg emissions and the restoration of Hg-polluted environments. One of the main focuses of the Minamata Convention is to address human-induced Hg releases to land and water, including setting release limits to reduce emissions from relevant sources. Given the strong correlation between riverine Hg and Hg release from human activities, riverine Hg fluxes and concentrations could serve as a rapid response metric to assess the effectiveness of Hg pollution governance and the effectiveness of the convention in watersheds where anthropogenic Hg releases are the major sources of the river, such as the Yangtze River (*12*, *15*).

Long-term monitoring could help to enhance our understanding of the sedimentation and resuspension of particulate Hg, as well as other riverine Hg processes. The 1850 Hg budgets and Hg concentrations could be considered as broad targets for Hg pollution governance. The simultaneous increase in background soil Hg concentrations and the influence of dams on riverine Hg delivery since the Industrial Revolution can be taken into account by MOSART for individual rivers. In addition, the 1850 Hg budgets and concentrations can still serve as a reference baseline, providing a historical benchmark to gauge the impacts of both natural and anthropogenic factors and the progress and effectiveness of Hg pollution reduction initiatives.

MATERIALS AND METHODS

Model platform

We use the MOSART-Hg to simulate the transport and fate of Hg in global rivers. This model is a part of the CESM2 (*32*, *61*). The river model is coupled with the Community Land Model 5.0 for Hg (CLM5-Hg). The model comprises a soil erosion module and a riverine sediment transport module, which are based on previously published code and studies from the Energy Exascale Earth System Model (E3SM) (*33*, *52*, *62*, *63*). This model allows us to simulate the processes of the transfer of Hg from soil to rivers and ultimately to oceans/lakes.

The structure of MOSART-Hg is illustrated in Fig. 3. After integrating the erosion module into CESM2, the processes and modules of CLM5 become connected to riverine Hg simulations. CLM5-Hg includes features from CLM5, such as vegetation processes, which can affect riverine Hg fluxes. For instance, vegetation changes can influence riverine Hg through their impact on erosion processes, as vegetation cover plays a crucial role in soil conservation. In addition, atmospheric forcing changes, CO_2 levels, and other parameters can affect Hg cycling on land. However, because of the simplified structure of MOSART, Hg cycling processes in rivers incorporate only sediment-based and liquid-based material flows. Without biogeochemical processes within the MOSART, transformations of Hg chemicals among its different forms in rivers are not considered. Instead, we assume that all riverine Hg exists in particulate form to simplify the modeling approach, following previous studies that have identified particulate phases as the dominant form of Hg in rivers (*12*, *13*, *19*). Given the limited sedimentation rates in river processes—where only 1% of riverine Hg is trapped—the uncertainties arising from the lack of Hg form transformations are estimated to be less than 1%.

To balance the model-resolving power and calculation efficiency, the CLM5-Hg is run at a resolution of 0.9° latitude × 1.25° longitude and the MOSART-Hg at 0.5° × 0.5°. The simulation is conducted from 1840 to 1859 to represent the riverine Hg processes in the preindustrial era. The first 5 years are used as spin-up (to initiate the model systems), while the subsequent 15 years are used for analysis. We ignore the atmospheric Hg deposition and the air-freshwater Hg exchange, as a preliminary calculation indicates their much smaller magnitudes than soil erosion.

We assume that soil Hg concentrations remain constant throughout the 20-year simulation, with initial soil Hg concentrations derived from Selin *et al.* (*30*). The spatial variability of soil concentrations is determined by assuming that each 4° × 5° model land grid square is in a yearly steady state (*30*). The spatial scaling factor used to represent the spatial heterogeneity of soil Hg concentration is determined iteratively. Starting from a uniform field set to 1, a 1-year preindustrial simulation is conducted. The factor is then locally adjusted for steady state, and this process is repeated over successive years until convergence (text S1).

The model is driven by the Global Soil Wetness Project Phase 3 (GSWP3) climate dataset at a horizontal resolution of 0.5°, spanning from 1901 to 1920 with a time resolution of 6 hours. This dataset is developed on the basis of the Climatic Research Unit -National Centers for Environmental Prediction (CRUNCEP) 6-Hourly Atmospheric Forcing Dataset (*64*), and the missing values for wind are filled on the basis of (*65*) that are interpolated by Climatological Data Atmosphere to the GSWP3 grid. This dataset includes the atmosphere-driving variables, such as precipitation, incoming solar radiation, temperature, pressure, wind speed, humidity, and downward longwave radiation. Specifically, the precipitation data play a crucial role in driving soil erosion, the water cycle, and river dynamics.

The present-day simulations account for processes related to human-induced Hg releases, trapping effects by dams, and other influencing factors. The former includes Hg sources from various sectors, such as industrial activities and ASGM (Fig. 3) (*26*). The magnitude of human-induced Hg releases is evaluated using observations and different scenarios, while the spatial distribution of Hg sources is based

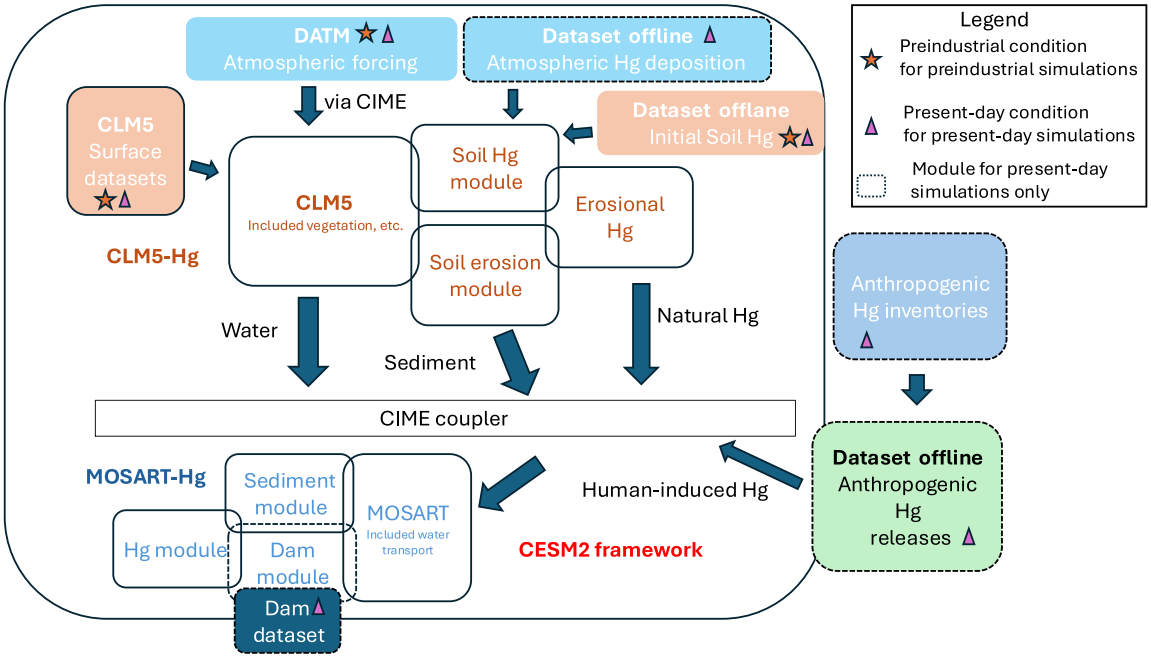

Fig. 3. Structure of MOSART-Hg. DATM, Data Atmosphere; CIME, Common Infrastructure for Modeling the Earth.

on the AMAP inventory (*66*, *67*) and the Streets inventory (*68*). The trapping effects of dams are represented through both process-based modeling and observational datasets. The trapping processes follow sediment dynamics described by Vörösmarty *et al.* (*69*) and Li *et al.* (*52*) and are integrated into Earth system models. The datasets are derived from the Global Reservoir and Dam database (*70*), with grid-based initialization following (*71*). Consequently, the spatial distribution of global riverine Hg is shaped by both Hg sources and dam construction. Dams act as barriers that reduce downstream and oceanic Hg fluxes, while anthropogenic Hg releases contribute to increased Hg levels in rivers.

CLM5-Hg

We add Hg modeling capacity to the CLM5 for the soil erosion module. The erosion module considers geographical and biogeochemical processes for Hg. The geographical processes are based on the improved Morgan model (*33*, *72*). This approach effectively represents soil erosion driven by precipitation and runoff. Specifically, the erosional Hg fluxes are calculated by erosional sediment flux times the soil Hg concentration in the corresponding grid cell. The performance of the estimation of the erosional sediment flux is validated in the previous studies (*33*, *54*). In addition, the soil erosion processes comprehensively consider the erosive impacts of throughfall and raindrops from the canopy (referred to as leaf drip power) and consider runoff-driven erosion. The soil particle detachment by raindrop impact F (in kilograms per square meter) is defined as

$$F_c = 10^{-3} K_c f_c (1 - ST)\left(KE_{DT} + KE_{LD}\right) \quad (1)$$

$$F_z = 10^{-3} K_z f_z (1 - ST)\left(KE_{DT} + KE_{LD}\right) \quad (2)$$

$$F_s = 10^{-3} K_s f_s (1 - ST)\left(KE_{DT} + KE_{LD}\right) \quad (3)$$

where F_c, F_z, and F_s are the clay, silt, and sand of soil detachment by rainfall F, respectively. The f_c, f_z, and f_s are the fractions of clay, silt, and sand particles in the surface soil, respectively; ST is the fraction of rock fragments on the soil surface; K is the erodibility of the soil (in grams per joule); and K_c, K_z, and K_s are the three soil erodibility parameters for clay, silt, and sand particles, respectively. The total energy of the effective rainfall (in joules per square meter) is the sum of the kinetic energy of the direct throughfall (KE_{DT}) and leaf drainage (KE_{LD}). KE_{DT} is determined as a function of the rainfall intensity I (in millimeters per hour) and the effective rainfall reaching the ground surface

$$KE_{DT} = R \times [(1 - CC) + CC \times (1 - A)] \times [11.87 + 8.73 \log_{10}(I)] \quad (4)$$

where R is the total rainfall (in millimeters), A is the fraction of the rainfall intercepted by the vegetation or canopy cover, and CC is the canopy cover fraction. The parameter KE_{LD} is estimated by

$$KE_{LD} = R \times CC \times A \times DR \times (15.8 PH^{0.5} - 5.87) \quad (5)$$

where PH is the height of the plant canopy (in meters), and DR is the fraction of leaf drainage.

The calculations of the soil detachment by runoff H (in kilograms per square meter) for clay, silt, and sand particles are calculated as

$$H_c = 19.1 \times 10^{-3} DR_c f_c Q_s^{1.5} \sin\theta \left[1 - \max(GC, ST)\right] \quad (6)$$

$$H_z = 19.1 \times 10^{-3} DR_z f_z Q_s^{1.5} \sin\theta [1 - \max(GC, ST)] \quad (7)$$

$$H_s = 19.1 \times 10^{-3} DR_s f_s Q_s^{1.5} \sin\theta [1 - \max(GC, ST)] \quad (8)$$

where DR_c, DR_z, and DR_s are the detachability of clay, silt, and sand particles by rain (in grams per millimeter), respectively. Q_s is the runoff (in millimeters), θ is the slope angle, GC is the fraction of ground cover, and ST is the fraction of rock fragments on the soil surface. We use the maximum value of GC and ST rather than their sum to avoid severely overestimating the protective effect of stone cover against erosion in forested areas (*33*).

We assume that the sediment transport in the runoff is only limited by the transport capacity. The transport capacity of runoff flow for three primary particles is given by

$$TC_c(Q_s) = 19.1 \times 10^{-3} f_v f_c Q_s^2 \sin(\theta) \quad (9)$$

$$TC_z(Q_s) = 19.1 \times 10^{-3} f_v f_z Q_s^2 \sin(\theta) \quad (10)$$

$$TC_s(Q_s) = 19.1 \times 10^{-3} f_v f_s Q_s^2 \sin(\theta) \quad (11)$$

where f_v is the adjustment factor of transport capacity due to the deviation from a standard flow velocity. We considered the effects of concentrated flow depth, vegetation, and stone covers on flow velocity

$$f_v = (d/0.005)^{0.67} e^{-0.018 \times ST} C \quad (12)$$

where C is the crop or plant cover factor, and d is the flow depth. The flux of eroded sediment to rivers is calculated as

$$Y_{sed} = \min(F + H, TC) \times CCoef \quad (13)$$

where Y_{sed} is the fluxes of erosional sediment to rivers (in kilograms per square meter), and $CCoef$ is a scaling factor to match the calculated flux with observed global riverine export of sediment (*17*, *20*). The input of soil Hg fluxes to rivers is calculated as

$$flux_{Hg} = Y_{sed} \times Conc_{Hg} \quad (14)$$

where $flux_{Hg}$ is the erosional Hg fluxes to rivers (in nanograms per square meter), and $Conc_{Hg}$ is the soil Hg concentration (in nanograms per kilogram). This method can also be applied to other sediment-based element cycling processes, such as particulate organic carbon.

MOSART-Hg

We model the Hg transport processes in rivers following that of sediment in the MOSART. The erosion fluxes of Hg predicted by CLM5-Hg are set as the input of the MOSART-Hg, in which the rivers are classified as hillslopes, subnetworks, and main channels to represent the confluence (*73*). The hillslopes are simulated by the Dominant River Tracing algorithm in MOSART (*62*). The sediment processes such as SPMs and wash loads are modeled following the MOSART sediment model developed by Li *et al.* (*52*). Nevertheless, the wash load processes of Hg are not taken into consideration due to the much lower Hg concentrations than the SPM. In addition, only particulate phase Hg is included in the MOSART-Hg model, as its dominant contribution to the total Hg content in riverine Hg budgets. The present-day river distribution is used because data on preindustrial river distribution are difficult to obtain following Syvitski and Kettner (*17*) and Syvitski *et al.* (*20*).

Considering the balance of simplicity and accuracy for sediment transport, we apply the revised Engelund-Hansen equation for Earth system models as the major equation to calculate the bed-material load of rivers (*52*), and the riverine Hg fluxes are embedded in the sediment fluxes. The total bed-material load Q_{total} (in kilograms per second) and Q_{Hg} (in grams per second) are calculated as

$$Q_{total,Hg} = \rho_{sed} \times B q^*_{total,Hg} \times \sqrt{R \times g \times D_{50}} \times D_{50} \quad (15)$$

where ρ_{sed} is the density of sediment (2650 kg/m^3), B is the channel width (in meters), R is submerged specific gravity for quartz in water (1.65), g is the gravity acceleration rate (9.8 m/s^2), D_{50} is the median grain size of bed-material sediment particles (in meters), and $q^*_{\text{total,Hg}}$ is the dimensionless total sediment flux per unit width for bed-material load (*52*). The suspended sediment and the rest settled fluxes are calculated as

$$Q_{sus} = Q_{total,Hg} \times \min\left(1, 2.5e^{-Z}\right) \quad (16)$$

$$Q_{settle} = Q_{total,Hg} - Q_{sus} \quad (17)$$

where Q_{sus} is the flux of suspended sediment (in kilograms per second), Hg (in grams per second), Z is the resuspension parameter (*52*), and Q_{settle} is the temporary storage part of the bed-material load in the river channel.

Sensitivity experiments

We conduct sensitivity experiments to assess the impact of finer resolution on mitigating model biases in simulating sediment fluxes, a crucial carrier of soil Hg from land to river systems. The accuracy of sediment flux representation is paramount in reducing biases in Hg flux simulations. We implement three scenarios: (i) a resolution of 1° (0.9° latitude × 1.25° longitude) run, (ii) a resolution of 0.5° (0.5° × 0.5°) run, and (iii) a constrained resolution of 1° run. The constrained resolution of 1° run is established on the basis of Eq. 13 to effectively mitigate the model bias. In addition, sediment flux records from other studies, representing prehuman, 1950, and present-day scenarios, are incorporated into the bias correlation analysis (*17*, *18*, *20*). Finer resolution provides enhanced detail in land topography, resulting in a more accurate sediment budget compared to available records (fig. S8). However, the finer resolution exhibits similar trends to the coarse resolution, indicating the reliability of the coefficient method (CCoef in Eq. 13) used in this study when compared to sediment records from other studies.

We address biases arising from Hg processes within land-river systems. Given the historical context of lower Hg deposition during the preindustrial era and limited gaseous Hg escape during soil Hg erosion and riverine delivery, we posit that the contribution of depositional Hg to erosional Hg fluxes is within ±5%, with gaseous Hg escape accounting for a 5% loss of erosional Hg flux (*25*, *48*, *74*). We establish three scenarios: (i) deposition plus 5%, (ii) escape loss 5%, and (iii) both considered or not considered. Evidently, the deposition and escape of Hg exhibit relatively lower biases in the model simulation (fig. S10). The actual impact of these two processes in the preindustrial era is less than 5% of the erosional flux.

Given the uncertainties stemming from soil Hg concentrations, we conduct sensitivity experiments encompassing a gradient of average global soil Hg concentrations (AGSHCs). Five scenarios of the Selin dataset (*30*) are established: (i) very high AGSHC at 50 ng/g (model + 15%), (ii) high AGSHC at 46.5 ng/g (+7.5%), (iii) model AGSHC at 43 ng/g, (iv) low AGSHC at 30 ng/g (−30%), and (v) very low AGSHC at 20 ng/g (−53%). The uncertainties arising from soil Hg concentrations are illustrated in fig. S9. We also designate the high soil Hg concentration scenario as the upper bound of model uncertainty ranges and the low scenario as the lower bound, with the model exporting 390 Mg/year (range: 321 to 483) of Hg to oceans during the simulation period.

We include the present-day soil Hg concentration datasets and the atmospheric forcing data in ~2000 to understand the uncertainties of the preindustrial simulation. Here, we use the soil Hg concentration datasets (referred to as the Wang dataset) from Wang *et al.* (*75*) and the atmospheric forcing data (GSWP3) during 1995–2004 to drive the preindustrial riverine Hg processes (details given in the table of fig. S1). The results of this sensitivity simulation are used as a reference, which represents the impact of climate (fig. S2). The differences between the Wang dataset (present-day soil Hg) and the Selin dataset (preindustrial soil Hg) reflect changes in soil Hg concentrations due to anthropogenic Hg releases and atmospheric Hg deposition. The AGSHC values represented by the Wang and Selin datasets are 47 ± 26 and 43 ng/g, respectively. In addition, changes in the atmospheric forcing data (GSWP3) from the preindustrial period (~1850) to the present day (atmospheric forcing data for simulation are from 1995 to 2004) reflect human-induced climate perturbations. Hence, from this experiment, we find that the combined impacts of increased soil Hg concentration (from 1850 to present day) and climate change (from 1850 to ~2000) have rather limited effects on the riverine Hg budgets (an increase of 30 Mg/year or 7% compared to preindustrial simulation; fig. S2).

Artificial intelligence assistance

We used ChatGPT-3.5 and 4o to assist in polishing the language and checking grammar. The prompts used were the following:

1) "You are now acting as an expert in the field of environmental science and biogeoscience. From a professional point of view, do you think there is any need to modify the below content? Be careful not to modify the whole text; you need to point out the places that need to be modified one by one and provide revision opinions and recommended revision content."

2) "Please help rewrite the following sentence and polish it into an academic tone."

Supplementary Materials

This PDF file includes:

Supplementary Text S1
Figs. S1 to S12
Tables S1 to S3
References

REFERENCES AND NOTES

1. F. Zahir, S. J. Rizwi, S. K. Haq, R. H. Khan, Low dose mercury toxicity and human health. *Environ. Toxicol. Pharmacol.* **20**, 351–360 (2005).
2. Q. Wu, Y. Zhang, P. Li, X. Fu, Q. Zhang, X. Wang, L. Chen, S. Wang, F. Wang, X. Feng, Ecosystem mercury recovery and health benefit under the minamata convention in a changing climate. *Rev. Environ. Contam. Toxicol.* **260**, 15 (2022).
3. AMAP/UNEP, "Technical Background Report for the Global Mercury Assessment 2018" (2019).
4. C. T. Driscoll, R. P. Mason, H. M. Chan, D. J. Jacob, N. Pirrone, Mercury as a global pollutant: Sources, pathways, and effects. *Environ. Sci. Technol.* **47**, 4967–4983 (2013).

5. M. Liu, Q. Zhang, C. Yu, L. Yuan, Y. He, W. Xiao, H. Zhang, J. Guo, W. Zhang, Y. Li, Q. Zhang, L. Chen, X. Wang, Observation-based mercury export from rivers to coastal oceans in East Asia. *Environ. Sci. Technol.* **55**, 14269–14280 (2021).
6. Y. Zhang, Z. Song, S. Huang, P. Zhang, Y. Peng, P. Wu, J. Gu, S. Dutkiewicz, H. Zhang, S. Wu, F. Wang, L. Chen, S. Wang, P. Li, Global health effects of future atmospheric mercury emissions. *Nat. Commun.* **12**, 3035 (2021).
7. C. Yu, H. Lin, J. Guo, M. Peng, M. Liu, Y. Tong, Y. Lu, X. Wang, X. Pan, Significant impacts of river inputs on the distributions and transports of mercury and methylmercury in nearshore and open seas – Simulation based on field surveys and mass balance modeling. *Environ. Int.* **180**, 108216 (2023).
8. D. Peng, Z. Liu, X. Su, Y. Xiao, Y. Wang, B. A. Middleton, T. Lei, Spatial distribution of heavy metals in the West Dongting Lake floodplain, China. *Environ. Sci. Process Impacts* **22**, 1256–1265 (2020).
9. D. Peng, M. Chen, X. Su, C. Liu, Z. Zhang, B. A. Middleton, T. Lei, Mercury accumulation potential of aquatic plant species in West Dongting Lake, China. *Environ. Pollut.* **324**, 121313 (2023).
10. E. Fluet-Chouinard, B. D. Stocker, Z. Zhang, A. Malhotra, J. R. Melton, B. Poulter, J. O. Kaplan, K. K. Goldewijk, S. Siebert, T. Minayeva, G. Hugelius, H. Joosten, A. Barthelmes, C. Prigent, F. Aires, A. M. Hoyt, N. Davidson, C. M. Finlayson, B. Lehner, R. B. Jackson, P. B. McIntyre, Extensive global wetland loss over the past three centuries. *Nature* **614**, 281–286 (2023).
11. C. A. Eagles-Smith, J. G. Wiener, C. S. Eckley, J. J. Willacker, D. C. Evers, M. Marvin-DiPasquale, D. Obrist, J. A. Fleck, G. R. Aiken, J. M. Lepak, A. K. Jackson, J. P. Webster, A. R. Stewart, J. A. Davis, C. N. Alpers, J. T. Ackerman, Mercury in western North America: A synthesis of environmental contamination, fluxes, bioaccumulation, and risk to fish and wildlife. *Sci. Total Environ.* **568**, 1213–1226 (2016).
12. M. Liu, Y. He, Z. Baumann, Q. Zhang, X. Jing, R. P. Mason, H. Xie, H. Shen, L. Chen, W. Zhang, Q. Zhang, X. Wang, The impact of the Three Gorges Dam on the fate of metal contaminants across the river–ocean continuum. *Water Res.* **185**, 116295 (2020).
13. P. F. Schuster, R. G. Striegl, G. R. Aiken, D. P. Krabbenhoft, J. F. Dewild, K. Butler, B. Kamark, M. Dornblaser, Mercury export from the Yukon River Basin and potential response to a changing climate. *Environ. Sci. Technol.* **45**, 9262–9267 (2011).
14. H. M. Horowitz, D. J. Jacob, H. M. Amos, D. G. Streets, E. M. Sunderland, Historical mercury releases from commercial products: Global environmental implications. *Environ. Sci. Technol.* **48**, 10242–10250 (2014).
15. D. Peng, J. Lyu, Z. Song, S. Huang, P. Zhang, J. Gao, Y. Zhang, Mercury budgets in the suspended particulate matters of the Yangtze River. *Water Res.* **243**, 120390 (2023).
16. J. Domagalski, M. S. Majewski, C. N. Alpers, C. S. Eckley, C. A. Eagles-Smith, L. Schenk, S. Wherry, Comparison of mercury mass loading in streams to atmospheric deposition in watersheds of Western North America: Evidence for non-atmospheric mercury sources. *Sci. Total Environ.* **568**, 638–650 (2016).
17. J. P. M. Syvitski, A. Kettner, Sediment flux and the Anthropocene. *Philos. Trans. R. Soc. A Math. Phys. Eng. Sci.* **369**, 957–975 (2011).
18. J. P. Syvitski, C. J. Vorosmarty, A. J. Kettner, P. Green, Impact of humans on the flux of terrestrial sediment to the global coastal ocean. *Science* **308**, 376–380 (2005).
19. H. M. Amos, D. J. Jacob, D. Kocman, H. M. Horowitz, Y. Zhang, S. Dutkiewicz, M. Horvat, E. S. Corbitt, D. P. Krabbenhoft, E. M. Sunderland, Global biogeochemical implications of mercury discharges from rivers and sediment burial. *Environ. Sci. Tech.* **48**, 9514–9522 (2014).
20. J. Syvitski, J. R. Ángel, Y. Saito, I. Overeem, C. J. Vörösmarty, H. Wang, D. Olago, Earth's sediment cycle during the Anthropocene. *Nat. Rev. Earth Environ.* **3**, 179–196 (2022).
21. M. Liu, Q. Zhang, T. Maavara, S. Liu, X. Wang, P. A. Raymond, Rivers as the largest source of mercury to coastal oceans worldwide. *Nat. Geosci.* **14**, 672–677 (2021).
22. C. Chandia, M. Salamanca, A. Hernández, R. Urrutia, Sediment mercury concentration changes as a response to increased industrial activity in Coronel Bay, Chile. *Mar. Pollut. Bull.* **178**, 113630 (2022).
23. M. Díaz-Asencio, C. M. Alonso-Hernández, Y. Bolanos-Álvarez, M. Gómez-Batista, V. Pinto, R. Morabito, J. I. Hernández-Albernas, M. Eriksson, J. A. Sanchez-Cabeza, One century sedimentary record of Hg and Pb pollution in the Sagua estuary (Cuba) derived from 210Pb and 137Cs chronology. *Mar. Pollut. Bull.* **59**, 108–115 (2009).
24. V. Hatje, R. L. B. Andrade, R. M. Jesus, P. Masqué, A. C. R. Albergaria-Barbosa, J. B. de Andrade, A. C. S. S. Santos, Historical records of mercury deposition in dated sediment cores reveal the impacts of the legacy and present-day human activities in Todos os Santos Bay, Northeast Brazil. *Mar. Pollut. Bull.* **145**, 396–406 (2019).
25. D. G. Streets, H. M. Horowitz, D. J. Jacob, Z. Lu, L. Levin, A. F. H. ter Schure, E. M. Sunderland, Total mercury released to the environment by human activities. *Environ. Sci. Technol.* **51**, 5969–5977 (2017).
26. D. Peng, Z. Tan, P. Wu, R. Chang, S. Huang, P. Zhang, Y. Wang, Z. Song, Y. Zhang, T. Lei, M. Liu, J. Gao, J. Liu, G. Lei, S. Tao, Mercury budget in global rivers at present-day: Impacts from reservoirs and dams. bioRxiv X55B0D [Preprint] (2025). https://doi.org/10.31223/X55B0D.
27. I. Devai, R. D. Delaune, G. Devai, C. Aradi, S. Gori, A. S. Nagy, Z. Talas, Characterization of mercury and other heavy metals in sediment of an ecological important backwater area of River Tisza (Hungary). *J. Environ. Sci. Health A Tox. Hazard. Subst. Environ. Eng.* **42**, 859–864 (2007).
28. S. Fornasaro, G. Morelli, P. Costagliola, V. Rimondi, P. Lattanzi, C. Fagotti, Total mercury mass load from the Paglia–Tiber River system: The contribution to Mediterranean Sea Hg budget. *Toxics* **10**, 395 (2022).
29. M. X. Bailon, A. S. David, Y. Park, E. Kim, Y. Hong, Total mercury, methyl mercury, and heavy metal concentrations in Hyeongsan River and its tributaries in Pohang City, South Korea. *Environ. Monit. Assess.* **190**, 274 (2018).
30. N. E. Selin, D. J. Jacob, R. M. Yantosca, S. Strode, L. Jaeglé, E. M. Sunderland, Global 3-D land-ocean-atmosphere model for mercury: Present-day versus preindustrial cycles and anthropogenic enrichment factors for deposition. *Global Biogeochem. Cy.* **22**, GB2011 (2008).
31. Y. Zhang, P. Zhang, Z. Song, S. Huang, T. Yuan, P. Wu, V. Shah, M. Liu, L. Chen, X. Wang, J. Zhou, Y. Agnan, An updated global mercury budget from a coupled atmosphere-land-ocean model: 40% more re-emissions buffer the effect of primary emission reductions. *One Earth* **6**, 316–325 (2023).
32. G. Danabasoglu, J. F. Lamarque, J. Bacmeister, D. A. Bailey, A. K. DuVivier, J. Edwards, L. K. Emmons, J. Fasullo, R. Garcia, A. Gettelman, C. Hannay, M. M. Holland, W. G. Large, P. H. Lauritzen, D. M. Lawrence, J. T. M. Lenaerts, K. Lindsay, W. H. Lipscomb, M. J. Mills, R. Neale, K. W. Oleson, B. Otto-Bliesner, A. S. Phillips, W. Sacks, S. Tilmes, L. van Kampenhout, M. Vertenstein, A. Bertini, J. Dennis, C. Deser, C. Fischer, B. Fox-Kemper, J. E. Kay, D. Kinnison, P. J. Kushner, V. E. Larson, M. C. Long, S. Mickelson, J. K. Moore, E. Nienhouse, L. Polvani, P. J. Rasch, W. G. Strand, The Community Earth System Model version 2 (CESM2). *J. Adv. Model. Earth Syst.* **12**, e2019MS001916 (2020).
33. Z. Tan, L. R. Leung, H. Y. Li, T. Tesfa, Modeling sediment yield in land surface and earth system models: Model comparison, development, and evaluation. *J. Adv. Model. Earth Syst.* **10**, 2192–2213 (2018).
34. K. L. Farnsworth, J. D. Milliman, Effects of climatic and anthropogenic change on small mountainous rivers: The Salinas River example. *Global Planet. Chang.* **39**, 53–64 (2003).
35. J. D. Milliman, J. P. M. Syvitski, Geomorphic/tectonic control of sediment discharge to the ocean: The importance of small mountainous rivers. *J. Geol.* **100**, 525–544 (1992).
36. J. Stelly, Y. Pokhrel, A. D. Tiwari, H. Dang, M.-H. Lo, D. Yamazaki, T.-Y. Lee, Reconstruction of long-term hydrologic change and typhoon-induced flood events over the entire island of Taiwan. *J. Hydrol. Reg. Stud.* **53**, 101806 (2024).
37. P. Billi, O. el Badri Ali, Sediment transport of the Blue Nile at Khartoum. *Quat. Int.* **226**, 12–22 (2010).
38. E. Garzanti, S. Andò, M. Padoan, G. Vezzoli, A. El Kammar, The modern Nile sediment system: Processes and products. *Quat. Sci. Rev.* **130**, 9–56 (2015).
39. R. Dubuis, G. De Cesare, The clogging of riverbeds: A review of the physical processes. *Earth Sci. Rev.* **239**, 104374 (2023).
40. W. F. Fitzgerald, D. R. Engstrom, C. R. Hammerschmidt, C. H. Lamborg, P. H. Balcom, A. L. Lima-Braun, M. H. Bothner, C. M. Reddy, Global and local sources of mercury deposition in coastal New England reconstructed from a multiproxy, high-resolution, estuarine sediment record. *Environ. Sci. Technol.* **52**, 7614–7620 (2018).
41. J. F. Gottgens, B. E. Rood, J. J. Delfino, B. S. Simmers, Uncertainty in paleoecological studies of mercury in sediment cores. *Water Air Soil Pollut.* **110**, 313–333 (1999).
42. P. M. Outridge, R. P. Mason, F. Wang, S. Guerrero, L. E. Heimbürger-Boavida, Updated global and oceanic mercury budgets for the United Nations Global Mercury Assessment 2018. *Environ. Sci. Technol.* **52**, 11466–11477 (2018).
43. M. Iturbide, J. M. Gutiérrez, L. M. Alves, J. Bedia, R. Cerezo-Mota, E. Cimadevilla, A. S. Cofiño, A. Di Luca, S. H. Faria, I. V. Gorodetskaya, M. Hauser, S. Herrera, K. Hennessy, H. T. Hewitt, R. G. Jones, S. Krakovska, R. Manzanas, D. Martínez-Castro, G. T. Narisma, I. S. Nurhati, I. Pinto, S. I. Seneviratne, B. van den Hurk, C. S. Vera, An update of IPCC climate reference regions for subcontinental analysis of climate model data: Definition and aggregated datasets. *Earth Syst. Sci. Data* **12**, 2959–2970 (2020).
44. A. Yoshimura, K. Suemasu, M. M. Veiga, Estimation of mercury losses and gold production by artisanal and small-scale gold mining (ASGM). *J. Sustain. Metall.* **7**, 1045–1059 (2021).
45. P. S. Soe, W. T. Kyaw, K. Arizono, Y. Ishibashi, T. Agusa, Mercury pollution from artisanal and small-scale gold mining in Myanmar and other Southeast Asian countries. *Int. J. Environ. Res. Public Health* **19**, 6290 (2022).
46. B. A. Zarcinas, C. F. Ishak, M. J. McLaughlin, G. Cozens, Heavy metals in soils and crops in Southeast Asia. *Environ. Geochem. Health* **26**, 343–357 (2004).
47. A. Gupta, "Erosion and sediment yield in Southeast Asia: A regional perspective," in *Erosion and Sediment Yield: Global and Regional Perspectives* (IAHS Publications, Series of Proceedings and Reports-Intern Assoc Hydrological Sciences, 1996), vol. 236, pp. 215–222.
48. D. G. Streets, M. K. Devane, Z. Lu, T. C. Bond, E. M. Sunderland, D. J. Jacob, All-time releases of mercury to the atmosphere from human activities. *Environ. Sci. Technol.* **45**, 10485–10491 (2011).

49. C. A. Cooke, A. Martínez-Cortizas, R. Bindler, M. Sexauer Gustin, Environmental archives of atmospheric Hg deposition – A review. *Sci. Total Environ.* **709**, 134800 (2020).
50. Y. Zhang, L. Jaegle, L. Thompson, D. G. Streets, Six centuries of changing oceanic mercury. *Global Biogeochem. Cy.* **28**, 1251–1261 (2014).
51. Z. Tan, L. R. Leung, H. Y. Li, T. Tesfa, Q. Zhu, M. Huang, A substantial role of soil erosion in the land carbon sink and its future changes. *Glob. Chang. Biol.* **26**, 2642–2655 (2020).
52. H.-Y. Li, Z. Tan, H. Ma, Z. Zhu, G. W. Abeshu, S. Zhu, S. Cohen, T. Zhou, D. Xu, L. R. Leung, A new large-scale suspended sediment model and its application over the United States. *Hydrol. Earth Syst. Sci.* **26**, 665–688 (2022).
53. H. Y. Li, L. R. Leung, A. Getirana, M. Y. Huang, H. Wu, Y. B. Xu, J. L. Guo, N. Voisin, Evaluating global streamflow simulations by a physically based routing model coupled with the community land model. *J. Hydrometeorol.* **16**, 948–971 (2015).
54. Z. Tan, L. R. Leung, H. Y. Li, S. Cohen, Representing global soil erosion and sediment flux in Earth system models. *J. Adv. Model Earth Syst.* **14**, e2021MS002756 (2022).
55. Y. Zhang, D. J. Jacob, S. Dutkiewicz, H. M. Amos, M. S. Long, E. M. Sunderland, Biogeochemical drivers of the fate of riverine mercury discharged to the global and Arctic oceans. *Global Biogeochem. Cycles* **29**, 854–864 (2015).
56. M. Bamford, D. Watkins, W. Bancroft, G. Tischler, J. Wahl, *Migratory Shorebirds of the East Asian – Australasian Flyway: Population Estimates and Internationally Important Sites* (Wetlands International, 2008).
57. J. S. Kirby, A. J. Stattersfield, S. H. M. Butchart, M. I. Evans, R. F. A. Grimmett, V. R. Jones, J. O'Sullivan, G. M. Tucker, I. Newton, Key conservation issues for migratory land- and waterbird species on the world's major flyways. *Bird Conserv. Int.* **18**, S49–S73 (2008).
58. A. Halls, *Wetlands, Biodiversity and the Ramsar Convention: The Role of the Convention on Wetlands in the Conservation and Wise Use of Biodiversity* (Ramsar Convention Bureau, 1997), vol. 13.
59. M. Chandler, *The Biodiversity Convention: Selected Issues of Interest to the International Lawyer*, Colorado Journal Of International Environmental Law And Policy (The University Press of Colorado, 1993), vol. 4.
60. R. Kessler, The Minamata Convention on Mercury: A first step toward protecting future generations. *Environ Health Perspect.* **121**, A304–a309 (2013).
61. L. K. Emmons, R. H. Schwantes, J. J. Orlando, G. Tyndall, D. Kinnison, J.-F. Lamarque, D. Marsh, M. J. Mills, S. Tilmes, C. Bardeen, R. R. Buchholz, A. Conley, A. Gettelman, R. Garcia, I. Simpson, D. R. Blake, S. Meinardi, G. Petron, The chemistry mechanism in the Community Earth System Model version 2 (CESM2). *J. Adv. Model. Earth Syst.* **12**, e2019MS001882 (2020).
62. H. Li, M. S. Wigmosta, H. Wu, M. Huang, Y. Ke, A. M. Coleman, L. R. Leung, A physically based runoff routing model for land surface and Earth system models. *J. Hydrometeorol.* **14**, 808–828 (2013).
63. Z. Tan, L. R. Leung, H. Y. Li, T. Tesfa, M. Vanmaercke, J. Poesen, X. S. Zhang, H. Lu, J. Hartmann, A global data analysis for representing sediment and particulate organic carbon yield in Earth system models. *Water Resour. Res.* **53**, 10674–10700 (2017).
64. N. Viovy, CRUNCEP version 7 – Atmospheric forcing data for the Community Land Model, Research Data Archive at the National Center for Atmospheric Research, Computational and Information Systems Laboratory (2018); https://doi.org/10.5065/PZ8F-F017.
65. T. Qian, A. Dai, K. E. Trenberth, K. W. Oleson, Simulation of global land surface conditions from 1948 to 2004. Part I: Forcing data and evaluations. *J. Hydrometeorol.* **7**, 953–975 (2006).
66. F. Steenhuisen, S. J. Wilson, Development and application of an updated geospatial distribution model for gridding 2015 global mercury emissions. *Atmos. Environ.* **211**, 138–150 (2019).
67. F. Steenhuisen, S. J. Wilson, Geospatially distributed (gridded) global mercury emissions to air from anthropogenic sources in 2015, DataverseNL (2022); https://doi.org/10.34894/SZ2KOI.
68. D. G. Streets, H. M. Horowitz, Z. Lu, L. Levin, C. P. Thackray, E. M. Sunderland, Global and regional trends in mercury emissions and concentrations, 2010–2015. *Atmos. Environ.* **201**, 417–427 (2019).
69. C. J. Vörösmarty, M. Meybeck, B. Fekete, K. Sharma, P. Green, J. P. M. Syvitski, Anthropogenic sediment retention: Major global impact from registered river impoundments. *Global Planet. Chang.* **39**, 169–190 (2003).
70. B. Lehner, C. R. Liermann, C. Revenga, C. Vörösmarty, B. Fekete, P. Crouzet, P. Döll, M. Endejan, K. Frenken, J. Magome, C. Nilsson, J. C. Robertson, R. Rödel, N. Sindorf, D. Wisser, High-resolution mapping of the world's reservoirs and dams for sustainable river-flow management. *Front. Ecol. Environ.* **9**, 494–502 (2011).
71. T. Zhou, L. R. Leung, G. Leng, N. Voisin, H. Y. Li, A. P. Craig, T. Tesfa, Y. Mao, Global irrigation characteristics and effects simulated by fully coupled land surface, river, and water management models in E3SM. *J. Adv. Model. Earth Syst.* **12**, e2020MS002069 (2020).
72. R. P. C. Morgan, J. H. Duzant, Modified MMF (Morgan-Morgan-Finney) model for evaluating effects of crops and vegetation cover on soil erosion. *Earth Surf. Process. Landf.* **33**, 90–106 (2008).
73. H.-Y. Li, L. R. Leung, A. Getirana, M. Huang, H. Wu, Y. Xu, J. Guo, N. Voisin, Evaluating global streamflow simulations by a physically based routing model coupled with the community land model. *J. Hydrometeorol.* **16**, 948–971 (2015).
74. G. S. da Silva, W. F. Jardim, P. S. Fadini, Elemental gaseous mercury flux at the water/air interface over the Negro River basin, Amazon, Brazil. *Sci. Total Environ.* **368**, 189–198 (2006).
75. X. Wang, W. Yuan, C.-J. Lin, L. Zhang, H. Zhang, X. Feng, Climate and vegetation as primary drivers for global mercury storage in surface soil. *Environ. Sci. Technol.* **53**, 10665–10675 (2019).
76. P. Panagos, M. Jiskra, P. Borrelli, L. Liakos, C. Ballabio, Mercury in European topsoils: Anthropogenic sources, stocks and fluxes. *Environ. Res.* **201**, 111556 (2021).
77. Y.-R. Liu, L. Guo, Z. Yang, Z. Xu, J. Zhao, S.-H. Wen, M. Delgado-Baquerizo, L. Chen, Multidimensional drivers of mercury distribution in global surface soils: Insights from a global standardized field survey. *Environ. Sci. Technol.* **57**, 12442–12452 (2023).
78. A. G. Lim, M. Jiskra, J. E. Sonke, S. V. Loiko, N. Kosykh, O. S. Pokrovsky, A revised pan-Arctic permafrost soil Hg pool based on Western Siberian peat Hg and carbon observations. *Biogeosciences* **17**, 3083–3097 (2020).
79. J. Shi, C. C. M. Ip, G. Zhang, G. Jiang, X. Li, Mercury profiles in sediments of the Pearl River Estuary and the surrounding coastal area of South China. *Environ. Pollut.* **158**, 1974–1979 (2010).
80. C. J. Sanders, I. R. Santos, E. V. Silva-Filho, S. R. Patchineelam, Mercury flux to estuarine sediments, derived from Pb-210 and Cs-137 geochronologies (Guaratuba Bay, Brazil). *Mar. Pollut. Bull.* **52**, 1085–1089 (2006).
81. A. C. Ruiz-Fernández, M. Rangel-García, L. H. Pérez-Bernal, P. G. López-Mendoza, A. Gracia, P. Schwing, D. Hollander, F. Páez-Osuna, J. G. Cardoso-Mohedano, T. Cuellar-Martinez, J. A. Sanchez-Cabeza, Mercury in sediment cores from the southern Gulf of Mexico: Preindustrial levels and temporal enrichment trends. *Mar. Pollut. Bull.* **149**, 110498 (2019).
82. B. Ouddane, N. Mikac, A. B. Cundy, L. Quillet, J. C. Fischer, A comparative study of mercury distribution and methylation in mudflats from two macrotidal estuaries: The Seine (France) and the Medway (United Kingdom). *Appl. Geochem.* **23**, 618–631 (2008).
83. D. R. Thévenot, R. Moilleron, L. Lestel, M.-C. Gromaire, V. Rocher, P. Cambier, P. Bonté, J.-L. Colin, C. de Pontevès, M. Meybeck, Critical budget of metal sources and pathways in the Seine River basin (1994–2003) for Cd, Cr, Cu, Hg, Ni, Pb and Zn. *Sci. Total Environ.* **375**, 180–203 (2007).
84. M. Meybeck, L. Lestel, P. Bonté, R. Moilleron, J. L. Colin, O. Rousselot, D. Hervé, C. de Pontevès, C. Grosbois, D. R. Thévenot, Historical perspective of heavy metals contamination (Cd, Cr, Cu, Hg, Pb, Zn) in the Seine River basin (France) following a DPSIR approach (1950–2005). *Sci. Total Environ.* **375**, 204–231 (2007).
85. S. Azoury, J. Tronczyński, J. F. Chiffoleau, D. Cossa, K. Nakhlé, S. Schmidt, G. Khalaf, Historical records of mercury, lead, and polycyclic aromatic hydrocarbons depositions in a dated sediment core from the Eastern Mediterranean. *Environ. Sci. Technol.* **47**, 7101–7109 (2013).
86. T. Leipe, M. Moros, A. Kotilainen, H. Vallius, K. Kabel, M. Endler, N. Kowalski, Mercury in Baltic Sea sediments—Natural background and anthropogenic impact. *Geochemistry* **73**, 249–259 (2013).
87. W. M. Fox, M. S. Johnson, S. R. Jones, R. T. Leah, D. Copplestone, The use of sediment cores from stable and developing salt marshes to reconstruct historical contamination profiles in the Mersey Estuary, UK. *Mar. Environ. Res.* **47**, 311–329 (1999).
88. S. K. Jha, S. B. Chavan, G. G. Pandit, S. Sadasivan, Geochronology of Pb and Hg pollution in a coastal marine environment using global fallout 137Cs. *J. Environ. Radioact.* **69**, 145–157 (2003).

Acknowledgments: We acknowledge the use of ChatGPT 3.5 and 4o for polishing the language. We thank K. Oleson, E. Kluzek, S. Levis, and the DiscussCESM Forum Community for the help. Any use of trade, firm, or product names is for descriptive purposes only and does not imply endorsement by the US Government. **Funding:** This work was funded by the National Natural Science Foundation of China (NNSFC) grant no. 42177349 (Z.S.), the Fundamental Research Funds for the Central Universities, China, grant nos. 0207–14380188 and 0207–14380168 (Z.S.), the "GeoX" Interdisciplinary Research Funds for the Frontiers Science Center for Critical Earth Material Cycling, Nanjing University (Z.S.), the Collaborative Innovation Center of Climate Change, Jiangsu Province (Z.S.), and the E3SM project of the Earth System Model Development program area of the Office of Science of the US Department of Energy (Z.T.). The Pacific Northwest National Laboratory is operated by Battelle for the US Department of Energy under contract no. DE-AC05-76RLO1830 (Z.T.). **Author contributions:** Writing—original draft: D.P., Y.Z., and P.W. Conceptualization: D.P. and Y.Z. Investigation: D.P. Writing—review and editing: D.P., Y.Z., J.G., Z.T., G.L., B.A.M., T.L., J.E.S., P.W., Z.S., and J.G. Methodology: D.P., Z.T., and P.Z. Resources: D.P., Y.Z., J.G., and G.L. Data curation: D.P. and Z.T. Validation: D.P., J.E.S., and G.L. Supervision: Y.Z. and J.G. Formal analysis: D.P., B.A.M., and J.E.S. Software: D.P., P.Z., T.Y., and S.H. Project administration: D.P. Visualization: D.P. **Competing interests:** The authors declare that they have no competing interests. **Data and materials availability:** All data needed to evaluate the conclusions in the paper are present in the paper and/or the Supplementary Materials. The datasets required for model simulations in this study

can be downloaded from the CESM2 repository (https://svn-ccsm-inputdata.cgd.ucar.edu/trunk/inputdata/) and the E3SM repository (https://web.lcrc.anl.gov/public/e3sm/inputdata/) by following the respective instructions and policies of CESM2 (www.cesm.ucar.edu/models/cesm2) and E3SM (https://e3sm.org/).

Submitted 16 January 2025
Accepted 2 May 2025
Published 11 June 2025
10.1126/sciadv.adw0471